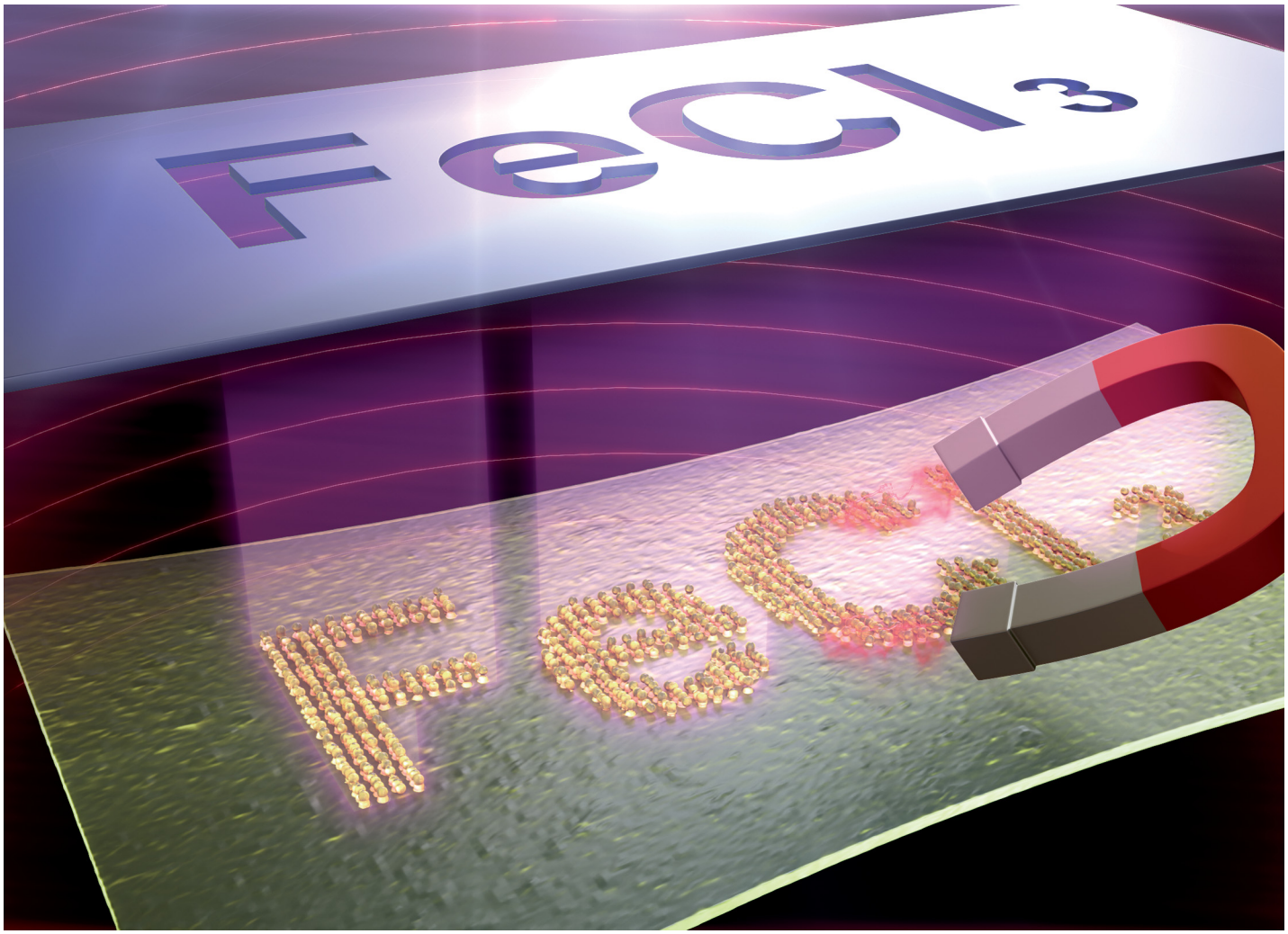

Showcasing collaborative research from Nihon University and Kanagawa University, Japan.

Development of a magnetic hybrid material capable of photoinduced phase separation of iron chloride by shape memory and photolithography

In this study, shape memory polymers and photodegradable iron complexes are used to control the phase separation of iron chloride. Iron chloride can partly be ordered and improve magnetic susceptibility.

As featured in:

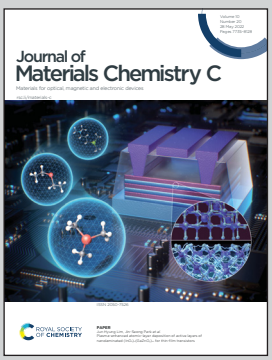

See Shuta Hara *et al.*,
J. Mater. Chem. C, 2022, **10**, 7849.

ROYAL SOCIETY OF CHEMISTRY

rsc.li/materials-c

Registered charity number: 207890

Journal of Materials Chemistry C

ROYAL SOCIETY OF CHEMISTRY

PAPER

View Article Online
View Journal | View Issue

Cite this: *J. Mater. Chem. C*, 2022, **10**, 7849

Development of a magnetic hybrid material capable of photoinduced phase separation of iron chloride by shape memory and photolithography†

Hiroki Ikake,[a] Shuta Hara,[*ab] Sei Kurebayashi,[a] Minami Kubodera,[a] Shota Watanabe,[a] Kazuto Hamada[a] and Shigeru Shimizu[a]

Received 21st December 2021,
Accepted 25th April 2022

DOI: 10.1039/d1tc06055d

rsc.li/materials-c

Magnetic material ordering is indispensable for improvement of magnetic susceptibility in limited polymer matrix space. In this study, a polymer matrix is designed to orient $FeCl_4^-$. As a result of this design, magnetic properties are observed in the hybrid material. However, partial control of magnetic susceptibility is important for practical applications of magnetic polymer materials. Here, $FeCl_3$ was partially ordered using a photodegradable Fe complex and a polymer having shape memory properties, in which uniaxial orientation of polymer segments causes a temporary shape. Although $FeCl_3$ was phase-separated from polymethyl methacrylate (PMMA), the complex composed of tetrabutylphosphonium cations and $FeCl_4^-$ anions (TBP[$FeCl_4$]) was uniformly dispersed in the PMMA matrix and produced $FeCl_3$ by photodegradation. Interestingly, $FeCl_3$ produced by photoreaction was ordered during shape recovery, from a temporary shape, due to phase separation of Fe oxide from the polymer matrix. Furthermore, UV light was partially irradiated on the sample using a photomask, to partially order the iron oxide. Hybrid samples of ordered $FeCl_3$ exhibited a 1.6 μm-interval striped pattern. These samples exhibited three times the magnetic susceptibility of disordered $FeCl_3$. This study makes contributions to the development of hybrid materials, incorporating inorganic materials into polymer matrix structures, thereby enhancing their properties, and utility.

Introduction

Polymers with magnetic properties exhibit flexibility and processability, unlike inorganic magnetic materials.[1–5] They have immense utility in magnetic storage media,[6,7] biomedical applications,[8–11] and separation functions.[12,13] Various strategies to incorporate magnetic properties into polymers, including addition of ferromagnetic nanoparticles,[14–16] and introduction of magnetic ionic liquid[17] into polymer side chains, have been proposed. Problems regarding phase separation, and structural uniformity of nanoparticles in the polymer matrix,[18–20] exist in the former, while the latter has limited practical applications due to its complicated synthetic methodology. However, magnetic ionic liquids (MILs) can be incorporated into versatile polymers by a simple process.[21,22]

[C4min][$FeCl_4$] was discovered as the first MIL by Hayashi *et al.*[23] In this material, the magnetic properties originate from anionic tetrahedral Fe halide complexes. Subsequently, various metal halides, such as $CoCl_2$, $MgCl_2$, and $GdCl_3$, have been analysed to fine-tune the magnetic properties of MILs.[24–26] These ionic liquids exhibit uniform paramagnetic behaviour[20–22] and their incorporation into general-purpose polymers produces transparent and paramagnetic hybrid polymers. This limitation is overcome by Fe–halogen complex ordering. Recent studies report improved magnetic susceptibility in magnetic polymers, due to Fe halide anion ordering by arrangement and self-assembly.[27–31] Yu *et al.* demonstrated superparamagnetic properties in oriented $FeCl_4^-$.[32] This property is derived from coupling of adjacent ordered Fe–halogen complexes using their spins. Partially tuning the magnetic susceptibility, rather than changing the magnetic susceptibility of the entire material, could enhance utility in magnetic storage media.[33–37]

The order of nanoparticles and polymer crystals in a polymer matrix is controlled by shape memory polymers (SMPs).[38–41] SMPs are an emerging class of intelligent materials that deform temporarily and change shape, but recover their original shape under environmental stimuli, such as heat,[42,43] light,[44,45] and an electric field.[46,47] When SMPs are uniaxially

[a] *Department of Materials and Applied Chemistry, College of Science and Technology, Nihon University, 1-8-14 Kandasurugadai, Chiyoda-ku, Tokyo 101-8308, Japan*
[b] *Department of Material and Life Chemistry, Kanagawa University, 3-6-1, Kanagawa-ku, Yokohama 221-8686, Japan. E-mail: ft102160vg@kanagawa-u.ac.jp*

† Electronic supplementary information (ESI) available: Results of shape memory programming by DMA, the shape memory process after UV irradiation, MFM after UV irradiation and shape recovery, XPS, and photographs before and after UV irradiation of the hybrid films. See DOI: https://doi.org/10.1039/d1tc06055d

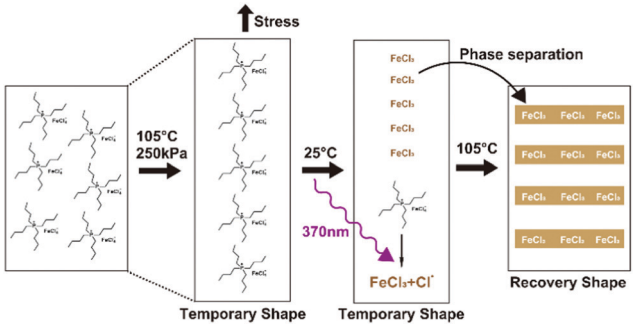

Fig. 1 Schematic representation of PMMA hybrid films with ordered $FeCl_3$, formed by combination of shape memory and a photodecomposition reaction.

stretched, the polymer segments are oriented, and this orientation is maintained by lowering the temperature, while maintaining constant stress. The orientation of this segment can maintain the orientation of the polymer crystals or the dispersion interval of the nanoparticles, in the polymer matrix. Therefore, SMPs containing MILs induce the ordering of the Fe ionic liquid when the SMP is uniaxially oriented.

In this work, Fe oxide was partially ordered by combining orientation properties of SMPs, with UV photodecomposition of the tetrabutylphosphonium cation and $FeCl_4^-$ complex (TBP[$FeCl_4$]) (Fig. 1). Previous publications report improvement of toughness and shape memory properties of titania-crosslinked PMMA-based hybrid network polymers on addition of tetrabutylphosphonium chloride (TBPC).[48,49] Quaternary phosphonium cations form complexes with various transition metal chlorides. Addition of Fe chloride to the PMMA/titania/TBPC system yielded a highly dispersed hybrid polymer with $FeCl_4^-$. In this study, decomposition of quaternary phosphonium by UV irradiation, in the presence of TBP[$FeCl_4$] was carried out. This generated $FeCl_3$ in the polymer matrix. The $FeCl_3$ underwent phase separation during shape recovery. Surprisingly, phase separation was ordered, and recorded as a striped pattern in the direction of extension, and perpendicular to it. Similar Fe oxide ordering was partially carried out using a photomask. $FeCl_3$ order was observed as a 1.6 μm-interval striped pattern by magnetic force microscopy (MFM). TBP[$FeCl_4$] decomposition by UV irradiation was analysed by UV-vis spectrometry, electron spin resonance (ESR), Fourier transform infrared spectroscopy (FTIR), and X-ray photoelectron spectroscopy (XPS). Magnetic properties of the $FeCl_3$-oriented hybrid materials were investigated by using a superconducting quantum interference device (SQUID). Ordered Fe oxide exhibited approximately twice the magnetic susceptibility of disordered $FeCl_3$.

Experimental

Materials

Methyl methacrylate (MMA), 3-(trimethoxysilyl) propyl methacrylate (MSi), 2,2-azobisisobutyronitrile (AIBN), and tetrabutylphosphonium chloride (TBPC) were purchased from Tokyo Chemical Industry Co. Ltd. Methanol, tetrahydrofuran (THF), *N*,*N*-dimethylformamide (DMF), hydrochloric acid (HCl), iron(III) chloride hexahydrate, cobalt(II) chloride hexahydrate, copper(II) chloride dihydrate, and zinc chloride were purchased from Kanto Chemical Co. Inc. Titanium isopropoxide (TiOPr) was purchased from Nippon Soda Co. Ltd.

Synthesis of Poly (MMA-*co*-MSi)

Poly(MMA-*co*-MSi) was synthesised according to a previous study.[48] Briefly, distilled MMA (17.73 g, 177.09 mmol), MSi (2.27 g, 9.307 mmol) (molar ratio MMA : MSi = 95 : 5), and 0.5 mol% AIBN (0.153 g, 0.932 mmol) were mixed in 60 mL of dehydrated DMF. The mixture was freeze–thawed to remove oxygen from the system and allowed to react for 4.5 h at 70 °C, followed by cooling to room temperature and addition of THF (30 mL). Precipitation purification was carried out twice with 800 mL of methanol. Precipitates were vacuum dried at room temperature for 24 h to obtain poly (MMA-*co*-MSi) (yield: 79.4%), and its THF gel permeation chromatography (GPC) analysis indicated a number average molecular weight (M_n) of 45 000 g mol^{-1} and M_w/M_n of 1.68.

Preparation of $FeCl_3$ composite hybrid films

Hybrid films were prepared according to a previous publication.[48,49] Poly(MMA-*co*-MSi) was dissolved in 80 mL of THF and added dropwise to a TiOPr (15 wt% based on the copolymer), TBPC (40 wt% based on the copolymer), and $FeCl_3$ (0, 5, 10 and 15 wt% based on the copolymer) solution. Subsequently, 25 μL of 1.0 M HCl was added dropwise to the mixture and stirred at 20 °C for 15 min. The solution was cast in a Petri dish and allowed to stand for 2 d at 25 °C, followed by 100 °C heat treatment for 90 min, in an Ar atmosphere, forming a hybrid film. Hybrid films were labelled Ti15TB40, Ti15TB40Fe5, Ti15TB40Fe10, and Ti15TB40Fe15, based on amount of $FeCl_3$ added. Films containing 40 wt% TBPC and 5 wt% $FeCl_3$ without TiOPr and hybrid films containing 15 wt% TiOPr and $FeCl_3$, without TBPC-labelled Ti0TB40Fe5 and Ti15TB0Fe5, respectively, were prepared using the method described, as control samples.

Preparation of oriented $FeCl_3$ composite hybrid films

Ti15TB40Fe5 was stretched up to 20% strain at 110 °C, and exposed to UV irradiation for 3 h. Subsequently, the external force was removed, producing oriented $FeCl_3$ composite hybrid films. Ti15TB40Fe5 films that were unprocessed, and treated with UV irradiation, and a shape memory process were labelled untreated, after UV, and structure samples, respectively.

Characterisation

Tensile tests of hybrid films were carried out with a testing speed of 30 mm min^{-1}, using an IM-20 (INTESCO Inc.). M_n and M_n/M_w of the copolymers were determined using an HLC-8220 GPC (Tosoh Co.) that was operated at 40 °C. The infrared (IR) spectra of the hybrid films were recorded on an FT/IR-6600 (JASCO Co.). Optical properties of the hybrid films were measured at room temperature with a scanning speed of

400 nm min^{-1}, using a UV-visible-near-infrared spectrophotometer V-670 (JASCO Corporation). Dynamic thermomechanical analysis (DMA) was performed using a DMS 6100 (Hitachi high technologies). Glass transition temperatures (T_g), and storage modulus values (E') of the hybrid films were measured in tension mode, with 1 Hz frequency, at a temperature range of 10–200 °C, a heating rate of 5 °C min^{-1}, and a nitrogen flow rate of 200 mL min^{-1}. Shape memory tests were carried out in stress-controlled thin film tension mode, with a 5 °C min^{-1} heating and cooling rate, and a 200 mL min^{-1} nitrogen flow rate. The nanoparticle elemental composition was analysed by monoatomic etching for Ar^+ ion energies, with 2 keV, using an Ar gas cluster ion beam, by XPS (ULVAC-PHI PHI 5000 VersaProbe III). An Ar ion gun was used for etching. Atomic force microscopy (AFM) and MFM were carried out using a NanoScopeV/Dimension Icon (Bruker AXS). The ESR spectra were recorded at −150 °C, using an X-band frequency of 9.23 GHz, by JES-RE2X (JEOL). The g value, representing an electron orbital state specific to a substance, was calculated by the following formula:

$$g = h\nu/\beta H_0$$

where h is Planck's constant, ν is microwave frequency, β is Bohr magneton, and H_0 is magnetic field. Magnetisation measurements were performed using an MPMS5 (Quantum Design Japan, Inc.).

Results

Characterization of TBP[$FeCl_4$]-containing hybrid films

Hybrid films, containing 40 wt% TBPC, 15 wt% TiOPr, and 5, 10, and 15 wt% $FeCl_3$, based on polymer weight, were fabricated to investigate the mechanical, thermodynamic, and shape memory properties on addition of $FeCl_3$ to PMMA/titania/TBPC. TG measurements were conducted to investigate the parenchymal content of titania in a previous study;[48] the Ti15TB40 sample contains approximately 10 wt% titania. Hybrid films containing 40 wt% TBPC, without $FeCl_3$ and those containing 15 wt% $FeCl_3$, without TBPC were prepared as samples for comparison. Fig. 1(a) shows photographs of hybrid films. The matrix containing TBPC exhibited high transparency, even on addition of 15 wt% $FeCl_3$, whereas the sample without TBPC exhibited low transparency, due to phase separation of $FeCl_3$. This indicated that TBPC aided compatibility of the $FeCl_3$ with the PMMA matrix. $FeCl_3$ was limited to 15 wt%, based on mass of PMMA, because addition of excess Fe caused ionic liquid leakage from PMMA, due to inhibition of weak TBPC carbonyl–PMMA bonds by strong $FeCl_3$ coordination. Fig. 2(b) shows stress–strain curves of the hybrid films. Fracture strain and stress of the hybrid materials did not exhibit significant variation with change in amount of $FeCl_3$. Hybrid film elongation was maximum for 5 wt% $FeCl_3$. The fracture energy of Ti15TB40Fe5 (1480.0 kJ m^{-3}) was approximately four times greater than the fracture energy of Ti15TB40Fe15 (375.8 kJ m^{-3}). Ti0TB40Fe5, without titania, had low Young's modulus, breakthrough strength, and elongation, compared to hybrid films containing titania. Fig. 2(b) shows E' and tan δ curves for hybrid films, without titania, without iron, and containing both (Ti0TB40Fe5, Ti15TB40Fe0, and Ti15TB40Fe5), at different temperatures. In the high-temperature region, E' exhibited a plateau for all films, due to a 3D network structure introduced by titania, with E' values in the plateau region independent of $FeCl_3$. The PMMA matrix behaved as an ideal chain in this region, and E' values were correlated with crosslink density. E' values of titania-free samples were lower than the E' of titania-containing samples. Table S1 (ESI†) summarises the tensile (Young's) modulus, tensile strength, brake energy, storage E' at 25 °C, and T_g values of the hybrid films. Addition of $FeCl_3$ did not affect the T_g values of the hybrid films from the peak of tan δ. An increase in TiOPr content increased the T_g values of the hybrid polymers, due to increase in the crosslink density. The TiOPr content was fixed at 15 wt% to minimise the effect of heat generated during UV irradiation on the hybrid films. Ti15TB40Fe5 was analysed using DMA and tensile tests. Ti15TB40Fe5, containing 5 wt% $FeCl_3$, was used, because Fe-containing hybrid films with higher amounts of $FeCl_3$ were brittle, and unsuitable for reproducible experiments.

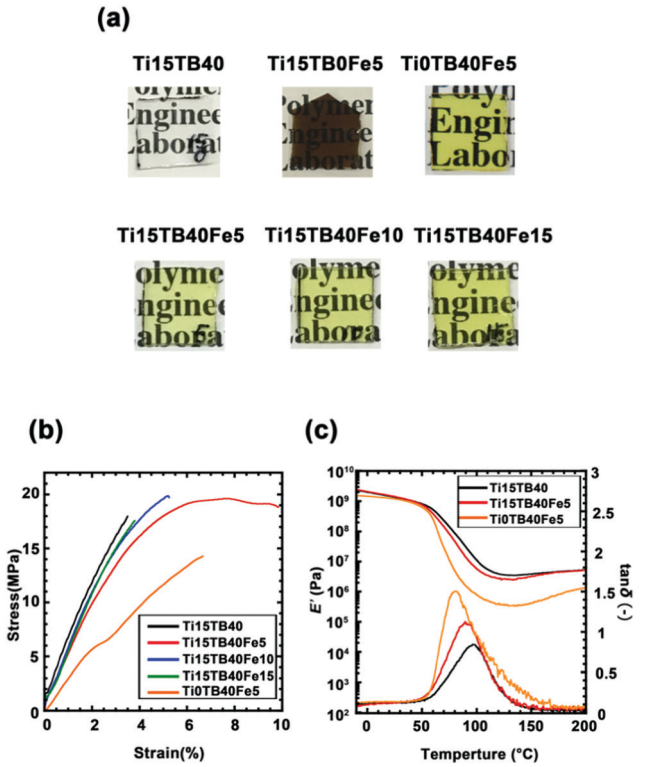

Fig. 2 (a) Images of hybrid co-PMMA/titania films: Ti15TB40, Ti15TB0Fe5, Ti0TB40Fe5, Ti15TB40Fe5, Ti15TB40Fe10, and Ti15TB40Fe15. (b) Stress–strain curves for co-PMMA hybrid films containing TBPC: Ti15TB40 (black line), Ti15TB40Fe5 (red line), Ti15TB40Fe10 (blue line), Ti15TB40Fe15 (green line), and Ti0TB40Fe5 (orange line). (c) DMA curves of hybrid films: Ti15TB40 (black line), Ti15TB40Fe5 (red line), and Ti0TB40Fe5 (orange line).

Morphology and magnetic properties of ordered $FeCl_3$ in hybrid polymers

Fig. 3(a) depicts the process for verifying Fe order. Shape memory characteristics of Ti15TB40Fe5 were evaluated using DMA (Fig. S1, ESI†). Shape fixing rate (Rf (96%)), shape recovery rate (Rr (92%)), maximum deformation rate (20%), and maximum stress (200 KPa), are summarized in Table S2 (ESI†). Shape memory processes for hybrid films were performed with 20% strain, and 200 KPa stress, with process details provided in the Supplementary Information (Fig. S2, ESI†). The UV irradiation process was completed in 1 h. Photographs of each execution process are shown in the ESI†, and photographs of the film during each process are shown in Fig. 3(b). The UV-irradiated sample turned brown, as shown in Fig. 3(b(ii)). However, only samples subjected to a shape memory process, as shown in Fig. 3(b(iii)), did not exhibit any change in state compared to the untreated samples (Fig. 3(b(i))). Thus, degradation of the TBP[$FeCl_4$] complex occurred only by UV irradiation, and not by heating. Films exposed to both UV irradiation, and a shape memory process, Fig. 3(b(iv)), turned brown, with colour being exhibited depending on the transmitted light. The morphology was investigated using a polarising microscope. Polarising microscope photographs of hybrid films are shown in Fig. 3(c). Only the film combining the shape memory process and UV irradiation exhibited a striped pattern. It was confirmed that the striped pattern was perpendicular to the distortion direction, indicated by black arrows in the figures. The distance between stripes was approximately 5 μm, and this striped pattern could be partially expressed using a photomask (Fig. 3(d)). The pattern exhibited sufficient resolution in the microscopic scale, without propagating. Thus, both light irradiation and the shape memory process were essential for streaks. Subsequently, to evaluate the structure and magnetic properties of the TBP[$FeCl_4$] decomposition product, AFM and MFM of the films exposed to UV irradiation (after UV samples), and those exposed to both UV irradiation and a shape memory process (structure samples), were measured. The striped pattern, observed by using a polarising microscope, could not be confirmed in both samples by AFM (Fig. 4(a) and (b)). A contrast of magnetic force could be confirmed by the shape having the striped pattern, under the condition of structure, in MFM. The MFM intensity profile indicated an average interval of 1.6 μm in the structure sample (Fig. S3(a) and (b), ESI†).

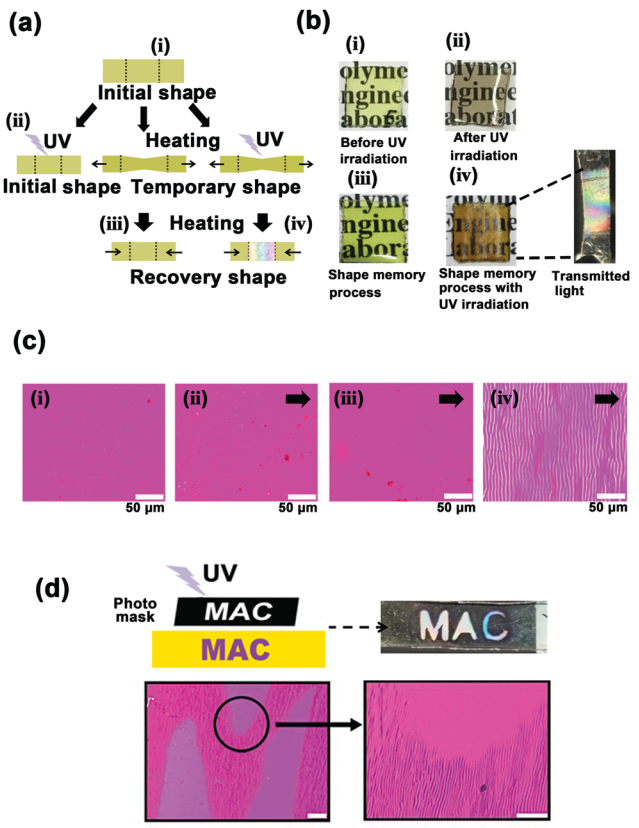

Fig. 3 (a) Preparation of $FeCl_3$-oriented hybrid films. Roman numerals represent different states of Ti15TB40Fe5: (i) Initial shape, (ii) after UV irradiation and 110 °C heating process, (iii) after shape memory process, and (iv) after UV irradiation and shape memory process. (b) Photographs of Ti15TB40Fe5 after each process and state, with (iv) expanded to show a photograph of transmitted light. (c) Microscope images of Ti15TB40Fe5 after each process. The white bar represents 50 μM. (d) Photographs of transmitted light and microscope image in the executed state of (iv), prepared by a photomask. The white bar represents 50 μM.

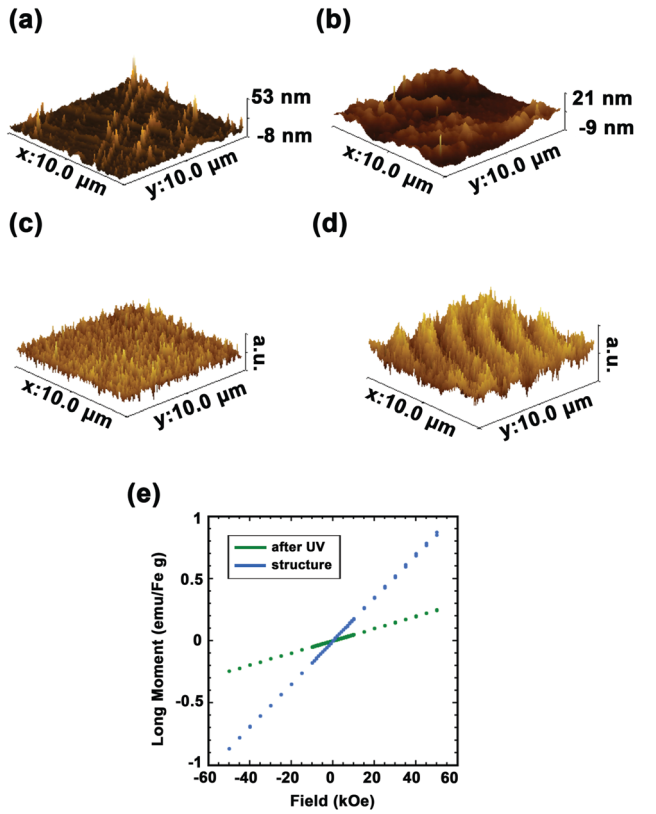

Fig. 4 AFM images of each state of Ti15TB40Fe5: (a) after UV irradiation, and (b) after UV irradiation and the shape memory process. MFM images of each state of Ti15TB40Fe5: (c) after UV irradiation, and (d) after UV irradiation and the shape memory process. (e) SQUID magnetometer measurements of Ti15TB40Fe5 after UV irradiation (green plot) and structure (blue plot).

Thus, the striped pattern, observed by the polarising microscope, was not caused by cracks in the polymer matrix, but by a decomposition product of TBP[$FeCl_4$]. To evaluate the structural effect of $FeCl_3$ on the magnetic susceptibility of the films, SQUID measurements were conducted on the after UV and structure samples. Both hybrid films exhibited paramagnetic behaviour, with magnetic susceptibility of 0.25 emu/Fe(g) and 0.85 emu/Fe(g), for the only UV process hybrid films and UV and shape memory process hybrid films, respectively, under 50 kOe external magnetic field. The magnetic susceptibility difference was more than three times, indicating the influence of $FeCl_3$ orientation on magnetic susceptibility.

Analysis of UV reaction products

UV reaction of TBP[$FeCl_4$] was investigated using UV-vis, IR, EDX, and XPS measurements. UV-vis measurements are shown in Fig. 5(a). Comparing untreated samples and Fe-free samples, absorption of TBP[$FeCl_4$] in Fe-containing samples was confirmed near 450 nm. Additionally, absorption around 450 nm was confirmed on films after the shape memory process, indicating no TBP[$FeCl_4$] decomposition due to the shape memory process at 105 °C. However, absorption around 450 nm was not confirmed in the after UV samples and structure samples, indicating TBP[$FeCl_4$] decomposition by UV irradiation. Absorption at approximately 450 nm is specific to TBP[$FeCl_4$]. The visible light transmittance of the structure samples was much lower than that of the after UV samples. This could be attributed to visible light scattering by the striped pattern, confirmed by a modified microscope, causing structural colour. IR spectral peaks at 2873 and 2932 cm^{-1} in untreated films, derived from CH of TBPC, disappeared in the after UV samples and structure sample films (Fig. 5(b)), indicating TBPC decomposition by UV irradiation. EDX measurements confirmed the state of Fe associated with TBPC decomposition (Fig. 5(c)). In the after UV samples, after one day, a peak (g) derived from Fe^{3+} was observed, which decreased after ten min. This indicated reduction of the Fe ion coordinated to the P cation, which could not be detected by ESR. The XPS spectra of Fe 2p of Ti15TB0Fe5 untreated samples, after UV samples, and structure samples, are shown in Fig. 5(d). Ti15TB0Fe5 untreated samples exhibited a broad peak at 710 eV, indicating the presence of Fe^0 and Fe^{3+}. On the other hand, the after UV samples and structure samples exhibited a peak at 707 eV, derived from Fe^0. Thus, Fe^{3+} was reduced to Fe^0 by UV irradiation. The XPS spectra of P 2p and Cl 2p are shown in Fig. S4 (ESI†). The Cl 2p peak did not exhibit any significant difference. In the P 2p peak, the peak at 132 eV was shifted to 134 eV, by UV irradiation. This indicated that UV irradiation oxidised the P atom of TBPC to produce P═O. Thus, Fe^{4+} was reduced to various valencies by oxidising P atoms, by UV irradiation, and subsequently oxidised to Fe^{3+} over time, with the Fe^0 state remaining partially unconverted.

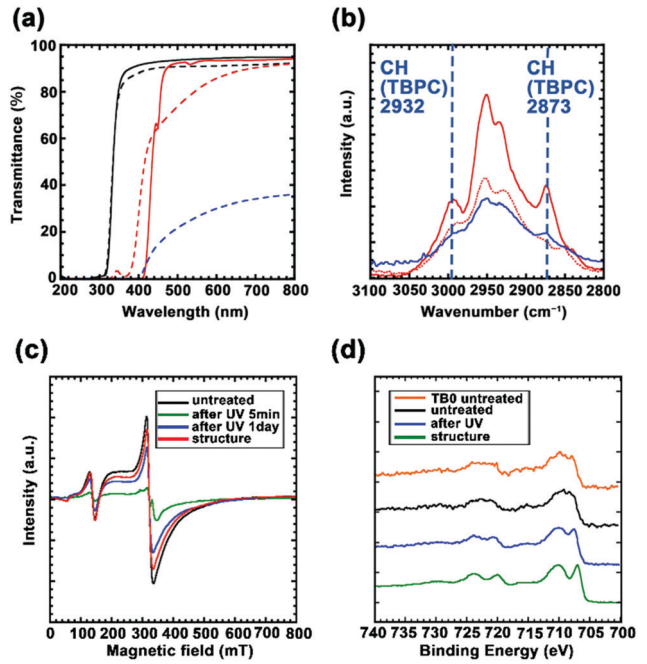

Fig. 5 (a) UV-vis spectra before (solid line) and after (dotted line) UV irradiation, for Ti15TB40 and Ti15TB40Fe5. Ti15TB40 (black line), Ti15TB40Fe5 (red line), and Ti15TB40Fe5 with UV irradiation and shape memory processes (blue plot). (b) FTIR spectra of Ti15TB40Fe5: untreated (red line), after UV irradiation (red plot), and structure (blue line). (c) ESR spectra of Ti15TB40Fe5: untreated (black line), after 5 min UV irradiation (green line), after 1 day UV irradiation (blue line), and structure (red line). (d) XPS spectra of Fe2p for Ti15TB0Fe5 and Ti15TB40Fe5: Ti15TB0Fe5 untreated (orange line), Ti15TB40Fe5 untreated (black line), Ti15TB40Fe5 after UV irradiation (blue line), and Ti15TB40Fe5 structure (green line).

Discussion

The titania/TBPC/PMMA hybrid system exhibited transparency and shape memory performance even after $FeCl_3$ addition. Transparency is a useful parameter to assess the dispersibility of titania, which correlates with the binding force between titania and the polymer side chains in this TBPC hybrid system.[49] For example, when the interaction between titania and the polymer side chain is weak, the transparency decreases and the film appears hazy. In the present system, the covalent bonding of the silane group to titania led to the high dispersibility of the latter, resulting in films with good transparency. Moreover, titania was used to adjust the Young's modulus at room temperature and to improve the E' value in the plateau region, which is vital for shape recovery. Lower E' values were observed in the plateau region of the sample without titania (Fig. 1(d)). The E' value in this region correlates with the crosslink density because the polymer behaves as an ideal chain.[48,49] The decrease in the crosslink density can be attributed to the reduced accessibility of the silyl group owing to the swelling of TBPC. Therefore, in this sol–gel reaction, the crosslink density of the swollen matrix can be adjusted by adding $Ti(OPr)_4$. In contrast, titania was not involved in the photoreaction of $FeCl_3$. $FeCl_3$ structuring was observed even in samples without titania. The addition of 10% excess $FeCl_3$ reduced the mechanical strength of the hybrid system. This could be due to

loss in ability of the TBPC's to block hydrogen bonds by $FeCl_3$ addition. In a previous study, TBPC was reported to improve the PMMA matrix toughness by blocking hydrogen bonds between PMMA side chain carbonyl groups, and titania. Xie *et al.*, and Estager *et al.* reported loss of $FeCl_4^-$ hydrogen bonding ability, produced by reaction of TBPC and $FeCl_3$. This loss was due to the nephelauxetic effect.[50,51] Here, the amount of $FeCl_3$ added was limited, considering the decrease in polymer matrix toughness, by the decrease in hydrogen bond shielding of TBPC, due to increase in precursor $FeCl_4^-$.

$FeCl_3$ was partially oriented perpendicular to the elongation direction, using optical lithographic techniques, with an angle of orientation related to the polymer uniaxial orientation in the primary shape state. In the sample without a shape memory process, the structure could not be confirmed with a microscope, or MFM, even after heating to T_g after UV irradiation. The controls and detailed mechanisms of ordering are currently under investigation, with polymer flow and the morphological state of the initial complex being essential factors. Here, the phase separation interval of $FeCl_3$ was 1.6 μm. This implies that control of the orientation interval requires improvement, because other phase separation methods produce nanoscale intervals.[52–54] However, partial orientation is a major advantage of this method and inducing such partial phase separation with typical polymer–polymer composites or polymer–nanoparticle composites is challenging. Additionally, the photomask, in terms of resolution, was well reproduced in the microscopic scale, and partial order of $FeCl_3$ improved the magnetic susceptibility by approximately 3.5 times. Several mechanisms have been proposed to improve the magnetic susceptibility of Fe complexes by structural control, including reduction of the Fe(III)–Fe(III) distance.[55–57] The range of Fe(III)–Fe(III) distances that affect magnetic susceptibility are estimated to be in Å units. Here, structures created were in the μm scale, and the coupling effect of Fe(III)–Fe(III) was not caused by structure, but by proximity of $FeCl_3$, compressed in single units of microstructure. In the future, further improvements in magnetic susceptibility could be investigated by controlling phase-separated structures in the nanoscale and using long-range coupling of $FeCl_3$ between structures.

Spectroscopic analysis indicated $FeCl_3$ production from the TBP[$FeCl_4$] precursor by photoreaction. It could be inferred that this UV-induced Fe reduction reaction began with Cl radicals generated by UV irradiation. Wu *et al.* reported photochlorination of cyclohexane using Fe chloride and copper chloride.[58] UV irradiation generated Cl radicals, with abstraction of one hydrogen atom from cyclohexane starting the reaction. The report considered that photoactivity is exhibited by metal chlorides with high valence, under oxidative conditions. The difference between the published report and this study is the abundance of tetrabutylphosphonium around chloride. The detailed reaction mechanism is currently under investigation, but Cl radicals could abstract hydrogen from tetrabutylphosphonium, generating a new P–Cl bond. Vetter *et al.* reported production of tributylphosphine chloride intermediates from Grignard reagents and phosphine oxide.[59] Here, instead of Grignard reagents, photoreactive $FeCl_4^-$ was a Cl source, producing P–Cl bonds and $FeCl_3$. The P–Cl bond being unstable, instantly reacted with oxygen to form phosphine oxide in the shape memory process (Fig. S4(a), ESI†). Additionally, to investigate the photoreaction of transition metal chlorides with TBPC, the tests conducted for $FeCl_3$ were repeated with other transition metal chlorides ($CoCl_2$, $NiCl_2$, $CuCl_2$, and $ZnCl_2$) (Fig. S5, ESI†). Only copper exhibited an apparent photodegradation behaviour. For $CuCl_2$, the structure could not be confirmed although the method of combining UV irradiation and the shape memory process was conducted (Fig. S6(c), ESI†). These results indicate that chloride radicals do not affect the crosslinked structure of PMMA and titania. The degradation of the crosslinked structure can induce the phase separation of titania. Therefore, this result supports that the observed structure in this case is not derived from the phase separation of titania. Moreover, CuCl produced by photolysis has a higher affinity for PMMA than $FeCl_3$, due to which the phase separation of copper cannot be confirmed. Similarly, the structures of other metal chlorides without the photodegradation behaviour could not be confirmed (Fig. S6(a), (b), and (d), ESI†). These results verify the working hypothesis that $FeCl_3$ that is decomposed by photoreaction is phase-separated from PMMA during shape recovery.

Conclusions

Uniform $FeCl_4$ mixing was observed using TBPC in a titania/PMMA system with the shape memory function. The addition of titania improved the crosslink density of the silane groups in the matrix swollen by TBPC. The amount of $FeCl_3$ added was limited to 5%, as excess addition inhibited the hydrogen bonding between PMMA and TBPC, thereby destabilising the complex. In this process, the agglomeration of $FeCl_3$ produced by photolysis was controlled using the fluidity of an SMP. The aggregated $FeCl_3$ has 1.6 μm intervals and has 3.4 times the magnetic susceptibility of random $FeCl_3$. Further improvements can be realised in this process through the investigation of the effect of the morphological state of the initial complex on the phase-separated structure. By controlling the initial dispersion density of the inorganic components, it is possible to construct a more optimal structure and improve its properties. This research proposes a method for constructing a structure bearing an inorganic component in a polymer matrix and can contribute to research aimed at improvement of the properties of inorganic components.

Author contributions

Conceptualization, S. H.; methodology, S. K.; investigation, M. K., S. W. and K. H.; writing – original draft preparation, S. H.; writing – review and editing, H. I.; supervision, S. S.; project administration, H. I. All the authors have read and agreed to the published version of the manuscript.

Conflicts of interest

There are no conflicts to declare.

Acknowledgements

The SQUID measurement was supported by the Nanotechnology Platform Program of MEXT, Grant Number JPMXP09 S20NI0032.

Notes and references

1 M. S. Ansari, M. H. D. Othman, M. O. Ansari, S. Ansari, H. Abdullah and Z. Harun, *J. Alloys Compd.*, 2020, **846**, 156368.
2 E. M. Palmero, J. Rial, J. de Vicente, J. Camarero, B. Skårman, H. Vidarsson, P. O. Larsson and A. Bollero, *Sci. Technol. Adv. Mater.*, 2018, **19**, 465.
3 J. Yuan, X. Qian, Z. Meng, B. Yang and Z. Q. Liu, *ACS Appl. Mater. Interfaces*, 2019, **11**, 17915.
4 E. Miękoś, M. Cichomski, M. Zieliński, T. Klepka, D. Sroczyński and A. Fenyk, *Materials*, 2021, **14**, 3806.
5 A. M. Majcher, P. Dąbczyński, M. M. Marzec, M. Ceglarska, J. Rysz, A. Bernasik, S. Ohkoshi and O. Stefańczyk, *Chem. Sci.*, 2018, **9**, 7277.
6 W. Cao, S. Yin, M. Plank, A. Chumakov, M. Opel, W. Chen, L. P. Kreuzer, J. E. Heger, M. Gallei, C. J. Brett, M. Schwartzkopf, A. A. Eliseev, E. O. Anokhin, L. A. Trusov, S. V. Roth and P. Müller-Buschbaum, *ACS Appl. Mater. Interfaces*, 2021, **13**, 1592.
7 A. A. Ahmad, A. M. Alsaad, Q. M. Al-Bataineh, M. H. Al-Akhras, Z. Albataineh, K. A. Alizzy and N. S. Daoud, *Polym. Bull.*, 2021, **78**, 1189.
8 J. Yunas, B. Mulyanti, I. Hamidah, M. M. Said, R. E. Pawinanto, W. A. F. W. Ali, A. Subandi, A. A. Hamzah, R. Latif and B. Y. Majlis, *Polymers*, 2020, **12**, 1184.
9 Ö. Lalegül-Ülkera and Y. M. Elçin, *Mater. Sci. Eng., C*, 2021, **119**, 111600.
10 S. Khizar, N. M. Ahmad, H. Saleem, M. A. Hamayun, S. Manzoor, N. Lebaz and A. Elaissari, *Adv. Polym. Technol.*, 2020, **2020**, 7163985.
11 M. A. Hassan, M. Saqib, H. Shaikh, N. M. Ahmad and A. Elaissari, *J. Biomed. Nanotechnol.*, 2013, **9**, 467.
12 Y. Sun, X. Ding, Z. Zheng, X. Cheng, X. Hua and Y. Peng, *Chem. Commun.*, 2006, 2765.
13 N. Soda, Z. J. Gonzaga, S. Chen, K. M. Koo, N. T. Nguyen, M. J. A. Shiddiky and B. H. A. Rehm, *ACS Appl. Mater. Interfaces*, 2021, **13**, 31418.
14 W. Cao, S. Yin, M. Plank, A. Chumakov, M. Opel, W. Chen, L. P. Kreuzer, J. E. Heger, M. Gallei, C. J. Brett, M. Schwartzkopf, A. A. Eliseev, E. O. Anokhin, L. A. Trusov, S. V. Roth and P. Müller-Buschbaum, *ACS Appl. Mater. Interfaces*, 2021, **13**, 1592.
15 Y. Li, Q. Liu, A. J. Hess, S. Mi, X. Liu, Z. Chen, Y. Xie and I. I. Smalyukh, *ACS Nano*, 2019, **13**, 13875.
16 H. Song, H. Lee, J. Lee, J. K. Choe, S. Lee, J. Y. Yi, S. Park, J. W. Yoo, M. S. Kwon and J. Kim, *Nano Lett.*, 2020, **20**, 5185.
17 C. Kaewsaneha, P. Tangboriboonrat, D. Polpanich, M. Eissa and A. Elaissari, *J. Polym. Sci., Part A: Polym. Chem.*, 2013, **51**, 4779.
18 C. Kaewsaneha, P. Tangboriboonrat, D. Polpanich, M. Eissa and A. Elaissari, *J. Colloid Interface Sci.*, 2013, **49**, 66.
19 C. Kaewsaneha, A. Bitara, P. Tangboriboonrat, D. Polpanich and A. Elaissaria, *J. Colloid Interface Sci.*, 2014, **424**, 98.
20 D. M. Correia, L. C. Fernandes, P. M. Martins, C. García-Astrain, C. M. Costa, J. Reguera and S. Lanceros-Méndez, *Adv. Funct. Mater.*, 2020, **30**, 1909736.
21 D. M. Correia, L. C. Fernandes, C. García-Astrain, M. Tariq, J. M. S. S. Esperança, V. de Zea Bermudeze and S. Lanceros-Méndez, *Composites, Part B*, 2019, **178**, 107516.
22 W. Xu, Q. Dai, Y. Wang, X. Hu, P. Xu, R. Ni and J. Meng, *RSC Adv.*, 2018, **8**, 21850.
23 S. Hayashi and H. Hamaguchi, *Chem. Lett.*, 2004, **33**, 1590.
24 A. N. Bowers, K. Santra, M. J. Trujillo-Rodríguez, A. Song, M. N. Emaus, J. W. Petrich and J. L. Anderson, *Anal. Bioanal. Chem.*, 2020, **412**, 2743.
25 H. Wang, Y. Jia, X. Wang, J. Ma and Y. Jing, *J. Chil. Chem. Soc.*, 2012, **57**, 1208.
26 M. A. Abdelaziz, F. R. Mansour and N. D. Danielson, *Anal. Bioanal. Chem.*, 2021, **413**, 205.
27 X. Yu, X. Yuan, Z. Xia and L. Ren, *Polym. Chem.*, 2018, **9**, 5116.
28 Z. Xia, X. Yu, T. Zhang, X. Yuan and L. Ren, *Polym. Chem.*, 2019, **10**, 4604.
29 W. Cañón-Mancisidor, P. Hermosilla-Ibáñez, E. Spodine, V. Paredes-García, C. J. Gómez-García, G. M. Espallargas and D. Venegas-Yazigi, *Cryst. Growth Des.*, 2021, **21**, 6213.
30 P. González-Izquierdo, O. Fabelo, L. Canadillas-Delgado, G. Beobide, O. Vallcorba, M. Sánchez-Andújar, M. T. Fernández-Díaz and I. de Pedro, *J. Mater. Chem. C*, 2020, **8**, 11389.
31 P. González-Izquierdo, O. Fabelo, L. Cañadillas-Delgado, G. Beobide, I. Cano, O. Vallcorba, J. R. Fernández, M. T. Fernández-Díaz and I. de Pedro, *J. Mol. Liq.*, 2021, **331**, 115716.
32 X. Yu, X. Yuan, Y. Zhao and L. Ren, *ACS Macro Lett.*, 2019, **8**, 1504.
33 S. Hara, S. Kurebayashi, G. Sanae, S. Watanabe, T. Kaneko, T. Toyama, S. Shimizu and H. Ikake, *Nanomaterials*, 2020, **11**, 5.
34 R. Zhang, B. Lee, M. R. Bockstaller, S. K. Kumar, C. M. Stafford, J. F. Douglas, D. Raghavan and A. Karim, *Macromolecules*, 2016, **49**, 3965.
35 H. Gu, S. W. Lee, J. Carnicelli, T. Zhang and D. Ren, *Nat. Commun.*, 2020, **11**, 2211.
36 I. C. Alard, J. Soubhye, G. Berger, M. Gelbcke, S. Spassov, K. Amighi, J. Goole and F. Meyer, *Polym. Chem.*, 2017, **8**, 2450.
37 W. Wu, M. Singh, A. Masud, X. Wang, A. Nallapaneni, Z. Xiao, Y. Zhai, Z. Wang, T. Terlier, M. Bleuel, G. Yuan, S. K. Satija,

J. F. Douglas, K. Matyjaszewski, M. R. Bockstaller and A. Karim, *ACS Nano*, 2021, **15**, 12042.
38 J. Wang, Q. Zhao, H. Cui, Y. Wang, H. Chen and X. Du, *J. Mater. Chem. A*, 2018, **6**, 24748.
39 P. Wu, X. Shen, C. G. Schäfer, J. Pan, J. Guo and C. Wang, *Nanoscale*, 2019, **11**, 20015.
40 W. Li, Y. Liu and J. Leng, *ACS Appl. Mater. Interfaces*, 2021, **13**, 23074–23080.
41 S. Shi, D. Shen, T. Xu and Y. Zhang, *Compos. Sci. Technol.*, 2018, **164**, 17.
42 A. Rybak, L. Malinowski, A. Adamus-Wlodarczyk and P. Ulanski, *Polymers*, 2021, **13**, 2191.
43 E. S. Keneth, R. Lieberman, M. Rednor, G. Scalet, F. Auricchio and S. Magdassi, *Polymers*, 2020, **12**, 710.
44 W. Miao, W. Zou, B. Jin, C. Ni, N. Zheng, Q. Zhao and T. Xie, *Nat. Commun.*, 2020, **11**, 4257.
45 C. Chu, Z. Xiang, J. Wang, H. Xie, T. Xiang and S. Zhou, *J. Mater. Chem. B*, 2020, **8**, 8061.
46 Y. C. Sun, M. Chu, M. Huang, O. Hegazi and H. E. Naguib, *Macromol. Mater. Eng.*, 2019, **304**, 1900196.
47 X. Gong, F. Xie, L. Liu, Y. Liu and J. Leng, *Polymers*, 2020, **12**, 387.
48 S. Hara, M. Ishizu, S. Watanabe, T. Kaneko, T. Toyama, S. Shimizua and H. Ikake, *Polym. Chem.*, 2019, **10**, 4779.
49 S. Hara, M. Tomono, K. Fukumoto, M. Kubodera, N. Kato, T. Kaneko, T. Toyama, S. Shimizu and H. Ikake, *ACS Appl. Polym. Mater.*, 2020, **2**, 5654.
50 Z. L. Xie, A. Jeličić, F. P. Wang, P. Rabu, A. Friedrich, S. Beuermann and A. Taubert, *J. Mater. Chem.*, 2010, **20**, 9543.
51 J. Estager, J. D. Holbrey and M. Swadźba-Kwaśny, *Chem. Soc. Rev.*, 2014, **43**, 847.
52 C. G. Bischak, C. L. Hetherington, H. Wu, S. Aloni, D. F. Ogletree, D. T. Limmer and N. S. Ginsberg, *Nano Lett.*, 2017, **17**, 1028.
53 S. Draguta, O. Sharia, S. J. Yoon, M. C. Brennan, Y. V. Morozov, J. S. Manser, P. V. Kamat, W. F. Schneider and M. Kuno, *Nat. Commun.*, 2017, **8**, 200.
54 W. Fan, Y. Shi, T. Shi, S. Chu, W. Chen, K. O. Ighodalo, J. Zhao, X. Li and Z. Xiao, *ACS Energy Lett.*, 2019, **4**, 2052.
55 P. González-Izquierdo, O. Fabelo, L. Cañadillas-Delgado, G. Beobide, O. Vallcorba, J. Salgado-Beceiro, M. Sánchez-Andújar, C. Martin, J. Ruiz-Fuentes, J. E. García, M. T. Fernández-Díaz and I. de Pedro, *J. Mater. Chem. C*, 2021, **9**, 4453.
56 J. A. DeGayner, K. Wang and T. D. Harris, *J. Am. Chem. Soc.*, 2018, **140**, 6550.
57 Y. Wang, M. E. Ziebel, L. Sun, J. T. Gish, T. J. Pearson, X. Z. Lu, A. E. Thorarinsdottir, M. C. Hersam, J. R. Long, D. E. Freedman, J. M. Rondinelli, D. Puggioni and T. D. Harris, *Chem. Mater.*, 2021, **33**, 8712.
58 W. Wu, Z. Fu, X. Wen, Y. Wang, S. Zou, Y. Meng, Y. Liu, S. Robert and K. D. Yin, *Appl. Catal., A*, 2014, **469**, 483.
59 A. C. Vetter, K. Nikitin and D. G. Gilheany, *Chem. Commun.*, 2018, **54**, 5843.

